Quartic multifractality and finite-size corrections at the spin quantum Hall transition

Martin Puschmann [1], Daniel Hernangómez-Pérez,[2] Bruno Lang,[3] Soumya Bera,[4] and Ferdinand Evers[1]

[1]*Institute of Theoretical Physics, University of Regensburg, D-93053 Regensburg, Germany*
[2]*Department of Molecular Chemistry and Material Science, Weizmann Institute of Science, Rehovot 7610001, Israel*
[3]*IMACM and Institute of Applied Computer Science, Bergische Universität Wuppertal, D-42119 Wuppertal, Germany*
[4]*Department of Physics, Indian Institute of Technology Bombay, Mumbai 400076, India*

The spin quantum Hall transition (or class C transition in two dimensions) represents one of the few localization-delocalization transitions for which some of the critical exponents are known exactly. Not known, however, is the multifractal spectrum τ_q, which describes the system-size scaling of inverse participation ratios P_q, i.e., the q moments of critical wave-function amplitudes. We here report simulations based on the class C Chalker-Coddington network and demonstrate that τ_q is (essentially) a quartic polynomial in q. Analytical results fix all prefactors except the quartic curvature that we obtain as $\gamma = (2.22 \pm 0.15) \times 10^{-3}$. In order to achieve the necessary accuracy in the presence of sizable corrections to scaling, we have analyzed the evolution with system size of the entire P_q-distribution function. As it turns out, in a sizable window of q values this distribution function exhibits a (single-parameter) scaling collapse already in the preasymptotic regime, where finite-size corrections are *not* negligible. This observation motivates us to propose new, original approach for extracting τ_q based on concepts borrowed from the Kolmogorov-Smirnov test of mathematical statistics. We believe that our work provides the conceptual means for high-precision investigations of multifractal spectra also near other localization-delocalization transitions of current interest, especially the integer (class A) quantum Hall effect.

I. INTRODUCTION

The Altland-Zirnbauer classification of disordered metals exhibits several symmetry classes that allow for insulating and metallic phases, which are separated by critical points or critical lines. Prominent examples include the integer, spin, and thermal quantum Hall effects in classes A, C, D or the Anderson transition in the symplectic class AII [1]. A distinguishing feature of these transitions is the statistics of the amplitudes of critical wave functions $\psi(\mathbf{r})$, which is conveniently described by their moments, i.e., the inverse participation ratios (IPR) $P_q(L) = \int d\mathbf{r}|\psi(\mathbf{r})|^{2q}$. For critical wave functions, the scaling of the average IPR with the system size L,

$$\overline{P_q}(L) \sim L^{-\tau_q}, \tag{1}$$

defines the set of multifractal exponents τ_q; the overline indicates a combined averaged over a narrow spectral window and an ensemble of disorder configurations ("samples").

The τ_q spectrum is of interest because it is a characteristic fingerprint of a critical state and the corresponding field theory. For instance, a long-standing conjecture by Zirnbauer [2] for the critical theory of the class A transition, which has undergone a recent refinement [3,4], implies that the multifractal spectrum takes a particularly simple form: τ_q is exactly parabolic in q. Therefore, the multifractal spectrum is a standard means to compare field-theoretical predictions and numerical simulations for microscopic models [1].

An important recent field-theoretic result [5–7] indicates that the spectrum τ_q for a transition in d dimensions has an exact representation

$$\tau_q = d(q-1) - qx_1 + x_q, \tag{2}$$

in terms of the exponents x_q that describe the scaling of the local density of states at criticality

$$\overline{\rho^q(\mathbf{r})} \sim L^{-x_q}. \tag{3}$$

Crucially, under very general conditions the exponents x_q obey a reciprocity relation [6–8]

$$x_q = x_{q^*-q}, \tag{4}$$

with q^* taking different values for different symmetry classes, e.g., $q^* = 1$ for class A and $q^* = 3$ for class C [6]. Even more intriguing is the result of Refs. [6,9–11] according to which reciprocity is a property not just of the exponents but of the entire correlator itself:

$$\overline{\rho^q(\mathbf{r})} = \overline{\rho^{q^*-q}(\mathbf{r})}, \tag{5}$$

in localized, delocalized, and critical regimes. This remarkable statement reflects a Weyl symmetry that is a property of the corresponding σ-model descriptions [6].

Inspired by the recent conjecture [3,4], in this paper we address the question of whether parabolicity of the multifractal spectrum could be a generic feature of quantum Hall transitions. Rather than investigating the class A transition considered by Zirnbauer *et al.* [3,4], we here focus on class C, i.e., the spin quantum Hall transition. Here, several open questions need to be addressed: (a) Taken at face value, the earlier numerical work on the class C transition suggests

pronounced deviations from parabolicity in the anomalous exponents $\Delta_q = \tau_q - d(q-1)$ [1,12]. At present, it cannot be safely excluded that the observed deviations are artifacts due to finite-size effects that have not been included in the earlier data analysis. Specifically, we have exact results for the local density of states (LDoS) exponent $x_1 = \frac{1}{4}$ and for the density correlator $x_2 = \frac{1}{4}$ [12,13]. Also at $q = 3$ an exact statement has been obtained corresponding to $x_3 = 0$ [12]. While all these results are consistent with the reciprocity condition $x_q = x_{3-q}$ and a putative parabolic form $x_q^{(\mathrm{p})} := \frac{1}{8}q(3-q)$, they are not sufficient to rule out quartic (and higher) terms in $q(q-3)$. (b) The validity of the reciprocity relation has not yet been established numerically for class C. (c) Further, we also address aspects of class C criticality that have received less attention in the past, most notably the set of tail exponents ζ_q that describes rare fluctuations with extremal IPR values.

There is one more consideration of a methodological kind that motivates us to scrutinize the class C transition once again. In contrast to class A, at the class C transition two non-trivial exponents are known analytically. This is very helpful for the analysis of simulation data because it gives reference points with respect to which finite-size effects can safely be quantified. We thus may use class C criticality as a laboratory to test known and explore novel approaches for fitting of critical exponents in the presence of sizable finite-size effects. In particular with an eye on open questions, e.g., in connection with the class A transition, such methodological advancements would certainly be welcome.

We briefly list our most important results obtained from simulations within the framework of the class C Chalker-Coddington network [13,14]:

(i) The reciprocity relation $x_q = x_{3-q}$ as well as the analytically predicted exponents are reproduced with excellent accuracy: $x_2 = 0.2504 \pm 0.0008$; $x_3 = 0.002 \pm 0.005$ (within an accuracy of 0.2%).

(ii) Quartic (and possibly higher) deviations from a parabolic shape $x_q^{(\mathrm{p})} = q(3-q)/8$ exist,

$$x_q = x_q^{(\mathrm{p})}[1 + 8\gamma_q(q-1)(q-2)],$$

with $8\gamma_q \approx 0.0178 \pm 0.0012$.

(iii) The tail exponents take values $\zeta_q \approx 2\zeta_2|q(q-1)|^{-1}$, $\zeta_2 = 4.5 \pm 0.5$ for $q \in [0, 3]$.

(iv) Within the framework of the σ model, i.e., by virtue of Eq. (5), the ratios

$$r_q(L) := L^{(d-x_1)(2q-q^*)} \frac{\overline{P_q}(L)}{\overline{P_{q^*-q}}(L)}, \qquad (6)$$

are not expected to exhibit corrections to scaling. Our data does not conform with this expectation; it exhibits discernible finite-size corrections $r_q(L) = r_q^*(1 + r_q^{(1)}L^{-y} + \cdots)$ with $y \approx 1$. Such corrections reflect microscopic features of lattice models that the coarse-grained scale of the σ model is ignorant of by design. In the present context they indicate that the σ model's Weyl symmetry is an emerging property.

(v) Traditionally, the ensemble-averaged IPR has received most of the attention because it is an object that appears naturally in quantum field theories [15] where it corresponds to a well-defined scaling operator. We here investigate the scaling properties of the entire IPR-distribution functions $\mathcal{P}_q$. Because

they are known to be more sensitive to finite-size effect, they lend themselves for sensing of these. Actually, we find that the distributions satisfy a nontrivial scaling relation

$$\mathcal{P}_q(\Lambda_q; L) = \frac{\lambda_q^*}{\lambda_q} \mathcal{P}_q^\infty\left(\frac{\lambda_q^*}{\lambda_q}\{\Lambda_q - c_q\} + c_q\right), \qquad (7)$$

valid within its bulk region; here, $\Lambda_q(L) = \ln P_q L^{\tau_q}$, λ_q^*, c_q constants, and $\lambda_q(L)/\lambda_q^* = 1 + O(L^{-y})$.

(vi) We propose a methodological advancement in the analysis of finite-size effects on the IPR scaling that relies on a standard parameter-free statistical test, the Kolmogorov-Smirnov test [16]. It allows to extract τ_q from the flow of the entire IPR distribution by fitting only a single parameter, even in the presence of significant finite-size correction.

II. MODEL AND METHODS

A. Model and method

We consider the version of the Chalker-Coddington network (CCN) [17] adapted to the spin quantum Hall transition (SQH) [13,14,18–20]. Since the model has been described extensively before [1,14], we allow ourselves to be brief. The class C network model consists of scattering nodes Σ arranged on a square lattice of size $L^2/2$ nodes. Neighboring nodes are connected by unidirectional links with opposing pairs incoming and outgoing. Every link carries two spin channels $\sigma \in \{\pm\}$ that mix while propagating along as prescribed by mixing matrices U_l, chosen at random from a SU(2) distribution but fixed for every link l. Nodal scattering for an incoming link is left or right; it is incorporated by orthogonal scattering matrices S diagonal in spin space $S^\Sigma = S_+^\Sigma \otimes S_-^\Sigma$. At criticality, scattering to the left and right occurs with the same probability $p = \frac{1}{2}$.

The network dynamics is mediated by the unitary network operator $\mathcal{U}$; it is the direct product of the mixing matrices U_l and the nodal scattering operators S^Σ, and it describes the evolution of the set of link probability amplitudes $\{\psi_{l+}, \psi_{l-}\}$, $l = 1, \ldots, L^2$, in discretized time [21,22]. The eigenvalues of $\mathcal{U}$ appear in pairs, $\exp(\pm i\epsilon)$. We construct $\mathcal{U}$ for a given disorder realization and use a variant of the Lanczos algorithm to extract six eigenstates $|\Psi\rangle$ corresponding to the three pairs of eigenvalues closest to unity. For the statistical analysis we employ one of the eigenvectors with eigenvalue closest to unity; the remaining two eigenstates are used as consistency check (see Appendix, Sec. A 3). We simulated networks with linear system sizes $L = 16, 24, 32, \ldots, 1024$ on a toroidal geometry and considered $\sim 10^7$ samples for the smallest and $\sim 10^6$ samples for the largest system size (see Appendix, Sec. A 1 for more details).

B. Observable

In lattice or network models there can be different microscopic observables that all flow towards the same macroscopic object after coarse graining. A typical example is the IPR in the CCN model, where the local weight per link can be, e.g., either $|\psi_+|^2$ or $|\psi_-|^2$ or the sum of both. All these local weights give rise to different flavors of the IPR. The difference will become manifest when rare events are considered:
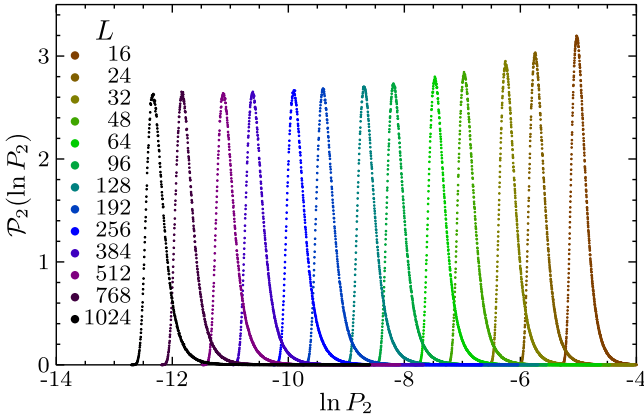
FIG. 1. Probability distribution $\mathcal{P}(\ln P_q, L)$ of the IPR for $q = 2$, presented for several system sizes $L = 16, \ldots, 1024$.

roughly speaking, a link with a particularly low weight is a lot more probable if just one amplitude is assigned to the link.

The weight we chose to implement is a physical observable, i.e., the occupation per link:

$$P_q(L) = \sum_l \left(\sum_\sigma |\psi_{l\sigma}|^2 \right)^q, \qquad (8)$$

with conventional normalization $P_1(L) = 1$. In the Appendix, Sec. A 4, we consider other flavors of IPR and show that the different weighting does not affect asymptotic scaling properties.

III. SELECTED PAIRS OF q VALUES

A. Finite-size effects at $q = 2$ and 3

We begin the presentation of our numerical results with the IPR at $q = 2$ and 3 because in these cases τ_q is known analytically: $\tau_2 = \frac{7}{4}$ and $\tau_3 = \frac{13}{4}$. Therefore, the irrelevant corrections to the scaling are readily exposed when considering *reduced* IPRs, $P_j L^{\tau_j}$ with $j = 2, 3$. The understanding here achieved we then will transfer to the case of general q values.

1. Case $q = 2$

Figure 1 shows the evolution ("flow") of the distribution function $\mathcal{P}_2$ of $\ln P_2(L)$ with system sizes. The typical behavior is seen: the distribution becomes shape invariant under shifting at largest system sizes. This shape invariance is generally considered to emerge only very close to the critical point [23]; therefore, the flow of the shape itself can be considered an indicator of the closeness to criticality and therefore is of interest to us, here.

To monitor the shape evolution we analyze the system-size dependency of its width

$$\sigma_q(L) = [\overline{[P_q(L) - \overline{P_q(L)}]^2}]^{1/2}, \qquad (9)$$

the result is displayed in Fig. 2. Another descriptor is the peak value $h_q(L)$ ("height") of the distribution, also shown in Fig. 2. Due to statistical fluctuations, $h_q(L)$ was obtained from polynomial fits to the distribution dome, applied at each
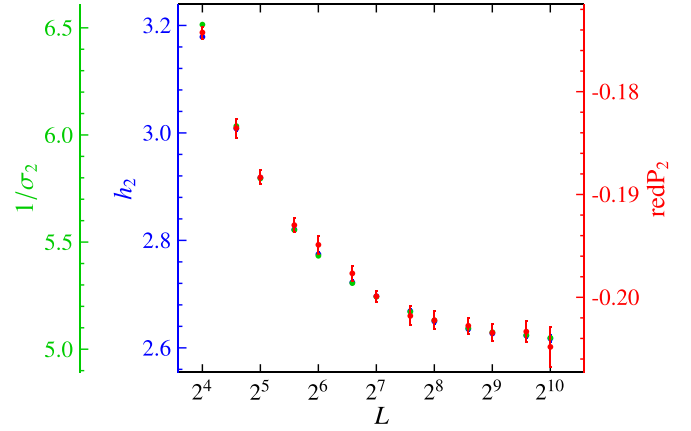

FIG. 2. Evolution of the shape of the IPR distribution $\mathcal{P}_2$ with increasing system size L, monitored by its width $\sigma_2(L)$ and height $h_2(L)$. Error bars represent statistical uncertainties due to random fluctuations and fluctuations based on fit ranges. Also shown is the residual shift of the maximum of the distribution of $\ln L^{\tau_2} P_2$ ("reduced distribution").

L separately. The fitting interval was identified by comparing the mean deviation for cubic and quartic fits. Due to normalization, the system-size variation of the inverse width $\sigma_q^{-1}(L)$ and the height $h_q(L)$ is identical in the limit of large L. Consequently, deviations from this behavior are indicative of preasymptotic changes in the shape of $\mathcal{P}_q$.

The growth of $\sigma_2(L)$ with increasing L in Fig. 2 accounts for the enhanced variability of local wave-function amplitudes, which in turn reflects the gradual unfolding of the localized character of the wave functions. Similar finite-size corrections as seen in height and width also manifest in the position and, hence, in the flow of the average IPR, $\overline{P_2}(L)$. For illustration we define the reduced peak position redP$_2(L)$, i.e., the position of the peak of the distribution of $\ln(L^{\tau_2} P_2)$. (The shifted argument implies subtracting the "translation" with L^{τ_2}.) For the reduced distribution $\mathcal{P}_2(\ln(P_2 L^{\tau_2}); L)$ a scaling collapse is expected in the limit $L \to \infty$ and indeed observed in Fig. 3. The corresponding peak position redP$_2(L)$ as extracted from Fig. 3 is also displayed in Fig. 2. Its saturation at
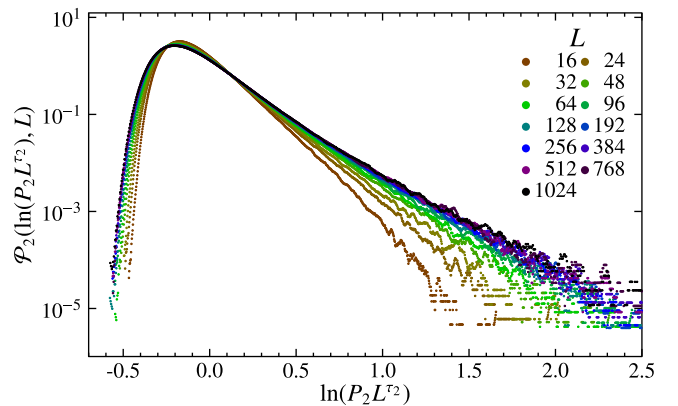

FIG. 3. Probability distribution $\mathcal{P}_2(\ln P_2 L^{\tau_2}, L)$ ("reduced distribution"). At large system sizes a scaling collapse is observed, indicating that the asymptotic scaling regime has been reached.
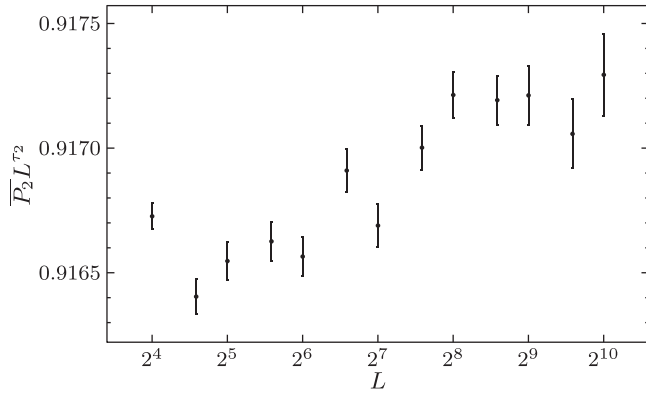
FIG. 4. Corrections to scaling for the reduced moment $\overline{P_2}L^{\tau_2}$ highlighting finite-size effects.

FIG. 5. Data analogous to Figs. 1 and 3, here for $q = 3$.

large L indicates that our data are indeed consistent with the expected theoretical exponent value.

A visual inspection of Fig. 2 suggests that the (inverse) width $1/\sigma_2(L)$ and the peak position $\mathrm{red}P_2(L)$ exhibit a concerted flow towards criticality. A more quantitative analysis proceeds by stipulating a form

$$\sigma_q(L) = \sigma_q^* \left(1 + \sum_{j=1}^{N_y} \sigma_q^{(j)} L^{-jy} \right), \quad (10)$$

and similar for $h_q(L)$ and $\mathrm{red}P_q(L)$. The specific form of the expansion is motivated by two facts: First, the IPR is a pure scaling operator [8], so that all observables deriving from it exhibit the same set of irrelevant exponents y. Second, we accommodate a single irrelevant scaling field, so only a single (irrelevant) exponent $y > 0$ appears. The details of the fitting procedure have been relegated to the Appendix, Sec. A 2. The extensive analysis yields two important conclusions: (i) good fits are obtained with $N_y = 2$; these fits are stable, in particular, against variations in the raw-data set and with $N_y = 1, 3$. (ii) The irrelevant exponent is obtained with best accuracy in the window $q \in [0, 2]$ where it takes values close to unity, $y = 1.0 \pm 0.2$.

Finite-size effects on the average IPR $\overline{P_2}(L)$ deserve a special attention. Remarkably, while the peak of the distribution function is seen to flow to the left in Fig. 3, an evolving power-law tail strengthens the right-hand side weight. Both effects cancel in the average $\overline{P_2}(L)$ to a surprising amount as seen in Fig. 4. It displays discernible, but weak finite-size corrections of the order of 0.1% within our window of system sizes.

For better understanding, we discuss the presence of finite-size corrections in $\overline{P_2}(L)$ in the light of the reciprocity relation (5). At $q=2$ we have the special situation that $L^{\tau_2}\overline{P_2}(L) = r_2(L)$, $\tau_2 = \frac{7}{4}$, since trivially $\overline{P_1}(L) = 1$. This is useful because the reciprocity relation implies that at least within the framework of the σ model the ratio $r_q(L)$ should not exhibit any scaling corrections, so also $L^{\tau_2}\overline{P_2}(L)$ is predicted to be independent of L. In Fig. 4 corrections to scaling are seen, however; actually, from a microscopic perspective this is hardly surprising since power laws are not expected to hold in the limit where L approaches the lattice constant.
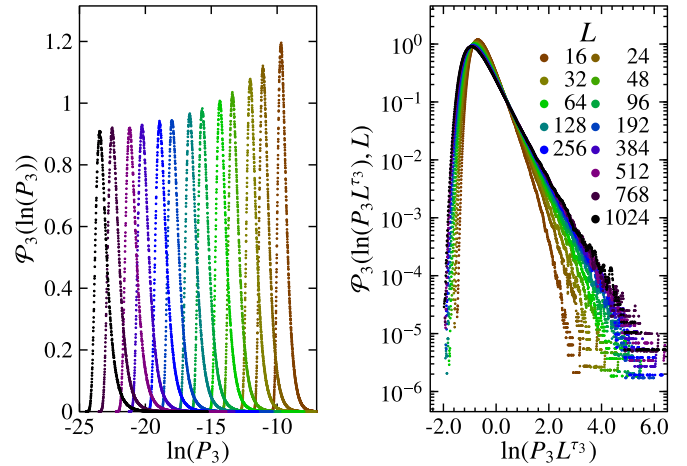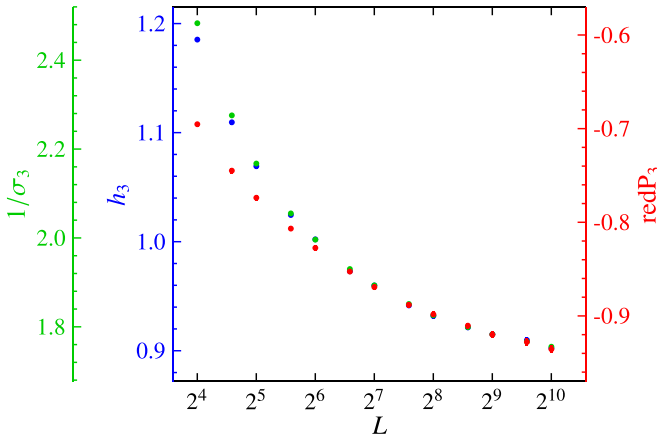
We elaborate on this observation: The σ model has a large (Weyl-type) symmetry; it eliminates corrections to scaling already at its short-distance cutoff, so that a field-theoretical perspective would predict a perfectly flat line in Fig. 4. We interpret our data deviating from flatness as an indication that the Weyl symmetry is, in principle, only approximate for microscopic models, such as the CCN. Consequently, lattice models can exhibit corrections to scaling also in observables that are correction free on the σ-model level. Conversely, the fact that corrections in Fig. 4 are seen to be so weak impressively illustrates how close the σ model is to microscopic representations of the class C transition.

The general importance of expansions such as Eq. (10) motivates one more remark. The corresponding expansion coefficients do not necessarily share the same sign. In fact, we show in the Appendix, Sec. A 2, Figs. 27 and 28 for the specific example of $\sigma_q(L)$ that the first coefficient $\sigma_q^{(1)}$ is likely negative, while the second one $\sigma_q^{(2)}$ is positive. As a consequence, the effects of the first and second correction terms partially cancel in a certain regime of system sizes ("conspiracy"), so that finite-size effects are very difficult to analyze. In the present situation this regime is narrow because $y \approx 1$, i.e., rather large; therefore, conspiracy is less relevant for the class C transition. Since y as reported [1,24] for the class A transition is much smaller, conspiracy is a more relevant issue for the integer quantum Hall effect.

2. Case $q = 3$

For $q = 3$ an analysis analogous to $q = 2$ can be performed based on the data shown in Fig. 5. Also in this case the gradual evolution of $\mathcal{P}_3(\ln P_3 L^{\tau_3}; L)$ terminates in a scaling collapse. The flow of the peak width $\sigma_3(L)$, height $h_3(L)$, and peak position $\mathrm{red}P_3(L)$ is depicted in Fig. 6. Its parametric analysis in terms of irrelevant corrections to scaling, Eq. (10), consolidates the picture developed above (see Appendix, Sec. A 2).

Also at $q = 3$ reciprocity predicts that the scaling corrections for $L^{\tau_3+d}\overline{P_3}(L)$, $\tau_3 + d = 21/4$, vanish on level of the σ-model description. We infer from Fig. 7 that the finite-size corrections seen in the microscopic model are pronounced, 10 times larger as compared to the case $q = 2$. The relative enhancement is not surprising: higher moments, i.e., larger q

FIG. 6. Data analogous to Fig. 2, here for $q = 3$.

values, probe more extreme wave-function amplitudes that are much more likely to occur in bigger systems.

B. Deviations from parabolic multifractality
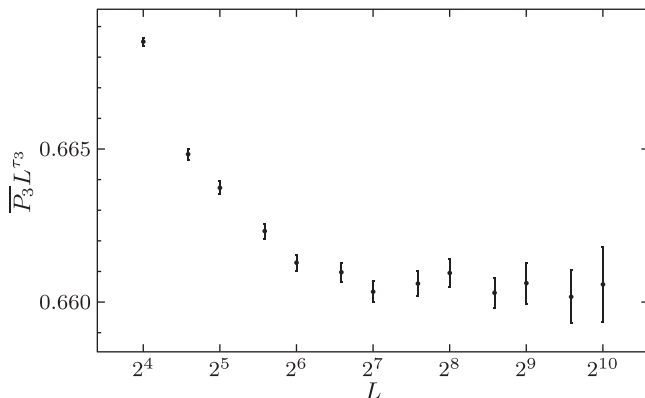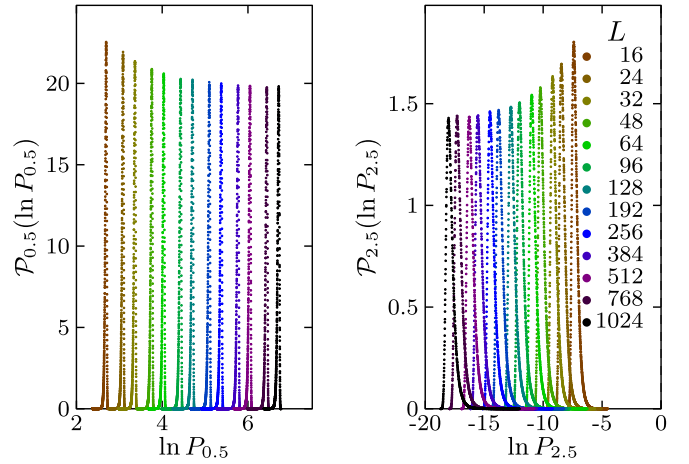
1. General considerations

After presenting an analysis of the structure of the finite-size corrections at the class C critical point, we now turn to the shape of the multifractal spectrum itself. Specifically, we will investigate potential deviations from a parabolic shape

$$\gamma_q := \frac{\tau_q - \tau_q^{(p)}}{q(q-1)(q^*-q)[q-(q^*-1)]},$$

$$= \frac{x_q - x_q^{(p)}}{q(q-1)(q^*-q)[q-(q^*-1)]}, \quad (11)$$

with $\gamma_q = \gamma_{q^*-q}$. For class C, $q^* = 3$ and $\tau_q^{(p)} := d(q-1) - q/4 + q(3-q)/8$. The first two factors in the denominator are standard [1]; they accommodate the trivial zeros of the numerator. The second two factors reflect the reciprocity symmetry; they appear in those universality classes for which q^* differs from unity. Obviously, we have $\gamma = 0$ for exact parabolicity.

It is implied by Eq. (11) that

$$x_q = \tfrac{1}{8}q(3-q)[1 + 8\gamma_q(q-1)(q-2)], \quad (12)$$

FIG. 7. Plot analogous to Fig. 4 highlighting finite-size effects in the reduced IPR, $\overline{P_3}L^{\tau_3}$, $\tau_3 = \frac{13}{4}$.

FIG. 8. Probability distribution $\mathcal{P}_q(\ln P_q, L)$ of the IPR for $q = \frac{1}{2}$ (left) and $q = \frac{5}{2}$ (right). System sizes: $L = 16, \ldots, 1024$.

while reciprocity symmetry suggests for the nonparabolicity parameter γ_q an expansion of the form

$$\gamma_q = \sum_{j=0} \gamma^{(j)}[(q - q^*/2)^2]^j. \quad (13)$$

Stipulating a weak dependency of γ_q on q, Eq. (12) suggests that deviations from parabolicity are relatively small within the window $q \in [1, 2]$ and more sizable outside. We therefore continue the analysis with the pair $q = \frac{1}{2}$, $\frac{5}{2}$.

2. Reciprocity pair $q = \frac{1}{2}$ and $\frac{5}{2}$

As in the previous cases of $q = 2$ and 3 we begin with an analysis of finite-size corrections visible in the raw data (see Fig. 8). Again we focus on a reduced IPR, which we now generalize to values away from $q = 2, 3$, so we investigate $L^{\tau_q^{(p)}} P_q(L)$. Our motivation is that in the presence of parabolicity one would expect a scaling collapse of $\mathcal{P}_q(L^{\tau_q^{(p)}} P_q(L))$. The flow of $\mathcal{P}_q$ of the reduced IPRs is parametrized in Fig. 9.

The first information summarized in the three panels is that the reciprocity pairs at largest system sizes exhibit an identical scaling with respect to corrections to the system size. This is best illustrated for the evolution of $h_q(L)$, but also $\sigma_q(L)$ is eventually seen to follow this trend. We take this as an evidence that above $L \approx 2^8 = 256$ the finite-size corrections are dominated by a single correction term L^{-y}. The second information is that beyond this scale $L \approx 256$ the reduced position $\mathrm{redP}_q(L)$ does not show a tendency settling towards a horizontal line. We interpret this observation as evidence that deviations to parabolicity exist.

Notice that these deviations as identified in Fig. 9 (inset, bottom panel) are consistent with reciprocity in the sense that redP_q, $q = \frac{1}{2}, \frac{5}{2}$ tend towards sharing the same slope; we highlight this important feature in Fig. 10 displaying the reduced average IPR for $q = \frac{1}{2}, \frac{5}{2}$. While finite-size corrections occur in both traces, the curves are seen to follow a common trend.
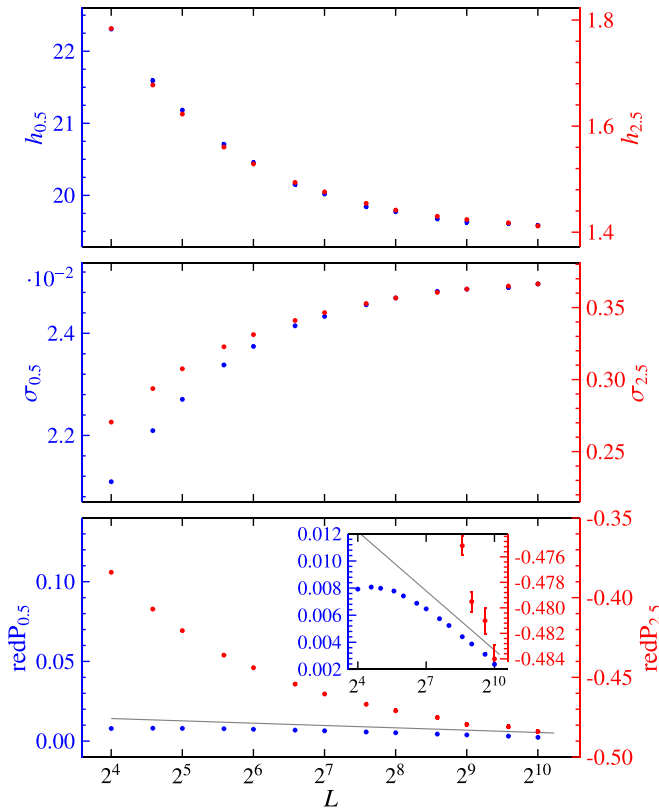
FIG. 9. Convergence of the height $h_q(L)$ (top panel), the width $\sigma_q(L)$ (middle), and the reduced peak position redP$_q(L)$ (bottom) for $q = \frac{1}{2}$ and $\frac{5}{2}$ with system size L. The inset shows the asymptotic region in which the peak positions shift in parallel for both q values, consistent with reciprocity. The solid line (slope corresponds to a γ value 0.002 244) is a guide to the eye indicating corrections to parabolicity in τ_q according to Eq. (12).

We remark that for $q = \frac{1}{2}$ the data in Fig. 10 exhibit a clear curvature to the right. In the case of parabolicity ($\gamma = 0$), the opposite trend is expected, i.e., a curvature to the left indicating a flow towards a horizontal line. We take this as further evidence that nonparabolicity, though numerically small, is a robust feature of our data.
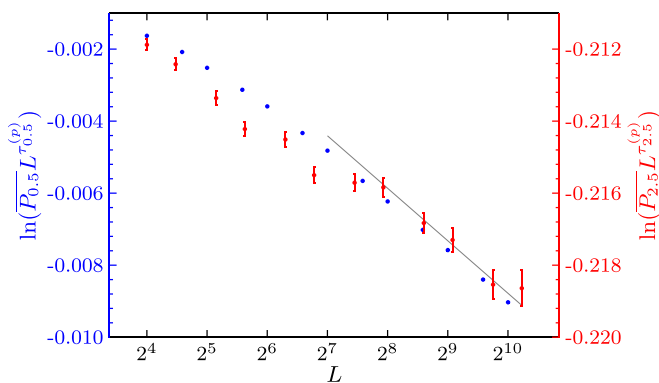

FIG. 10. Average IPR reduced by parabolic scaling relation for the reciprocity pair $q = \frac{1}{2}$ and $\frac{5}{2}$ as function of the system size L. The line is a guide to the eye with slope corresponding to a γ value of 0.002 244.
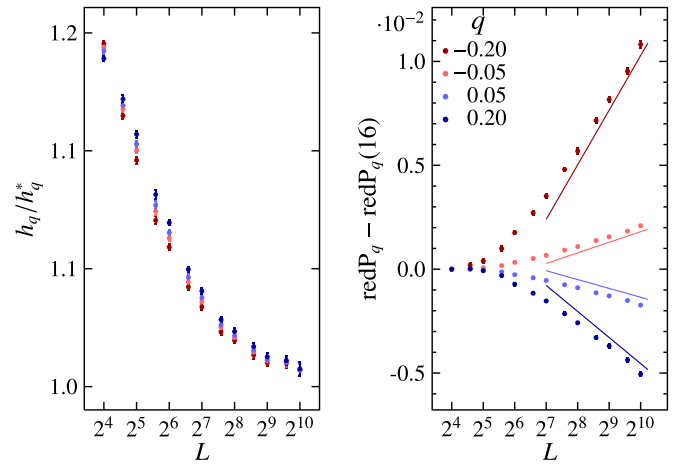

FIG. 11. Data analogous to Fig. 2 for $q = \pm\frac{1}{20}, \pm\frac{1}{4}$. Left panel: normalized distribution height h_q/h_q^* as function L. The asymptotic value h_q^* is 19.32, 89.35, 29.85, 99.47 for $q = \pm\frac{1}{5}, \pm\frac{1}{20}$, respectively. Right panel: shift of the peak position with system size L. The solid lines guide eye; the slopes correspond to a γ value 0.002 244.

3. Case $q \approx 0$

We continue the analysis with a moment near zero, i.e., $q = \pm\frac{1}{20}$ and $\pm\frac{1}{4}$, at which according to (12) corrections to parabolicity are expected to become even stronger than at $q = \frac{1}{2}$. Due to the increased statistical uncertainty of the symmetry partners $q = \frac{59}{20}, \frac{11}{4}$, we here focus on the small-q regime. The trend that has announced itself already at $q = \frac{1}{2}$ here consolidates: In Fig. 11 the height $h_q(L)$ shows a fast convergence behavior that has a counterpart in the reduced position redP$_q(L)$, only if a residual flow, and hence deviations from parabolicity, are admitted. The scaling of the reduced average IPR, $\overline{P}_q(L)$, confirms this picture (see Fig. 12).

4. Case of $q \in [1, 2]$

As the final discussion of individual q values we consider the symmetry point $q = \frac{3}{2}$ and the pair $q = \frac{5}{4}, \frac{7}{4}$ around it as representatives of the region $q \in [1, 2]$. The characteristic flow parameters are given in Fig. 13.
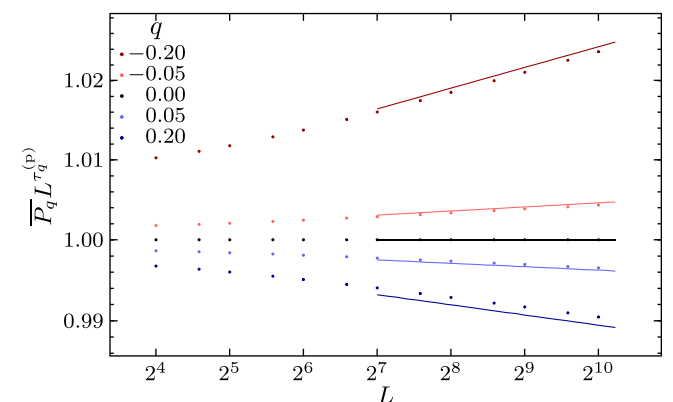

FIG. 12. Plot similar to Fig. 4 for $q = \pm\frac{1}{20}, \pm\frac{1}{4}$ and $q = \pm\frac{1}{4}$ in logarithmic scale for both axes. Solid lines guide the eye with slope corresponding to a γ value 0.002 244.
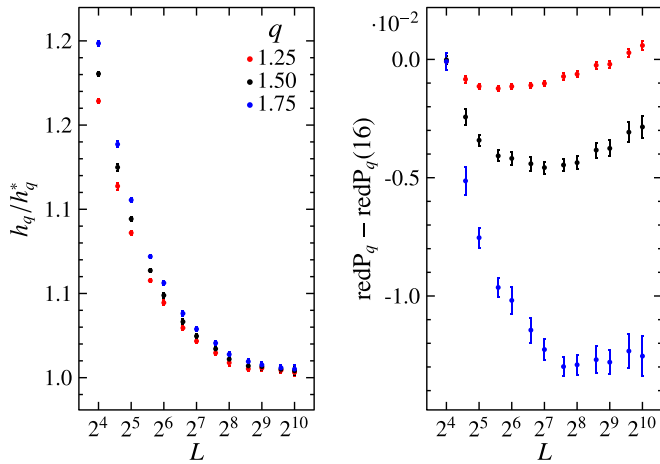
FIG. 13. Normalized distribution height h_q/h_q^* (left panel) and relative shift of the peak position of the reduced distribution redP_q (right panel) as function of L for $q = \frac{5}{4}, \frac{3}{2}, \frac{7}{4}$. Error bars represent statistical uncertainties due to limited ensemble averaging and fluctuations based on fit ranges. The asymptotic value h_q^* is 16.35, 6.848, 3.942 for $q = \frac{5}{4}, \frac{3}{2}, \frac{7}{4}$, respectively.

The flow of $h_q(L)$ [and similar also for $\sigma_q(L)$, not shown] exhibits the familiar convergence consistent with $y \approx 1$. In contrast, the reduced shift behaves in a nonmonotonous way, which by itself does not suggest converged behavior. The situation becomes clear after consulting Fig. 14. It shows that the traces for $q = \frac{5}{4}, \frac{7}{4}$ take the same slope at $L \gtrsim 300$, i.e., in the regime where $h_q(L)$ saturates. The nonvanishing slope is a manifestation of nonparabolicity. Also, it is seen that the trace corresponding to $q = \frac{3}{2}$ is intersecting with the other traces exhibiting a larger slope. From this trace we extract $\gamma_{3/2} = 0.002\,20 \pm .000\,05$ consistent with the other estimates.
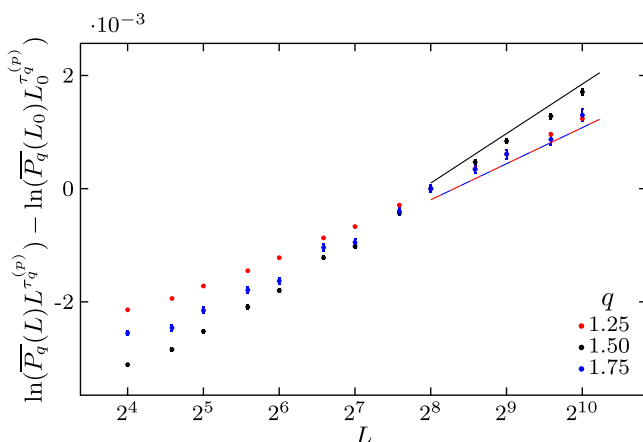

FIG. 14. Average reduced IPR for $q = \frac{5}{4}, \frac{3}{2}, \frac{7}{4}$ in log representation of both axes. The reference scale $L_0 = 2^8 = 256$ is the beginning of the asymptotic regime as indicated from the overlapping traces of the reciprocity pair $q = \frac{5}{4}, \frac{7}{4}$ and the convergence of the peak shape (see Fig. 13). The asymptotic slope indicates deviations from parabolicity, i.e., $\Delta x_q := x_q - x_q^{(\text{p})}$. The asymptotic collapse of $q = \frac{5}{4}, \frac{7}{4}$ reflects the symmetry with respect to $q = \frac{3}{2}$. Solid lines guide the eye.
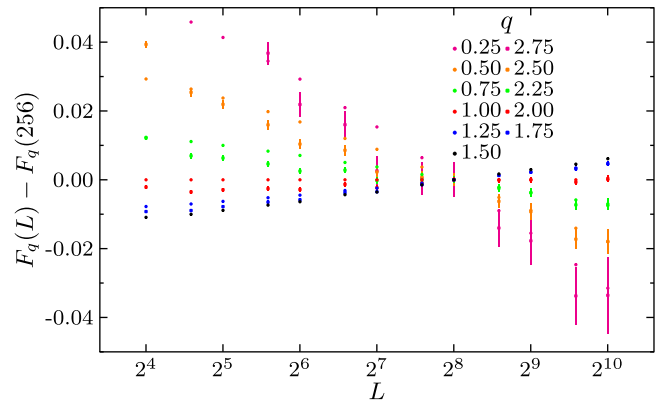

FIG. 15. The function F_q defined in Eq. (14). At system sizes $L \gtrsim L_0$, $L_0 = 256$ it displays the expected collapse of reciprocity pairs.

IV. ASYMPTOTICS OVER THE FULL SPECTRAL RANGE

We extend the findings made for selected q values over the entire range.

A. IPR scaling and hypercollapse

For a global description of the IPR, we define a function

$$F_q(L) := 8 \ln[\overline{P}_q(L)\, L^{\tau_q^p}]/[q(3 - q)]. \tag{14}$$

$F_q(L)$ is expected to scale as

$$
\begin{aligned}
F_q(L) &\approx F_q(L_0) + \frac{x_q - x_q^{(\text{p})}}{q(3 - q)/8} \ln L/L_0 \\
&= F_q(L_0) + 8\gamma(q - 1)(q - 2) \ln L/L_0,
\end{aligned}
$$

where L_0 denotes a reference length that indicates the beginning of the asymptotic scaling regime. The numerical data corresponding to $F_q(L)$ is displayed in Fig. 15 with $L_0 = 256$. At $L \approx L_0$ two traces that correspond to q values paired via the reciprocity symmetry $x_q = x_{3-q}$ coalesce within the numerical error bars that represent statistical noise. By analyzing the scaling of the entire distribution function we have argued before that this is also the system size that indicates the onset of the asymptotic scaling regime. Therefore, we interpret the slope of $F_q(L)$ seen at $L > L_0$ in Fig. 15, upper panel, as an evidence for the existence of nonparabolic corrections in τ_q.

For quantitative estimates of nonparabolicity, we employ the scaling ansatz separately for each q with fixed (universal) y:

$$\overline{P}_q(L) L^{\tau_q^p} = L^{-\Delta \tau_q} \sum_{j=1}^{N_y} a^{(j)} L^{-jy}. \tag{15}$$

By varying the fit initial conditions, we ensure the convergence to a global minimum. With this approach, we created several sets by manually varying the fit range N_y, and especially y. For the latter we considered values between 0.1 and 1.5. For these data sets we compared the overall fit quality and checked the quality of the numerical agreement with the exact values for $q = 2$ and 3 ($\Delta \tau_2 = \Delta \tau_3 = 0$). In particular, $\Delta \tau_3 = 0$ provides a strong figure of merit to discriminate between values of y. Based on the current data, we observe
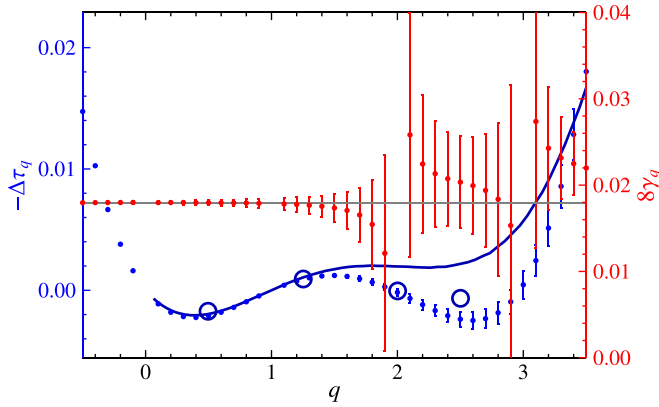
FIG. 16. Estimate of $\Delta\tau_q$ and corresponding γ_q as a function of q. Fits are based on $\overline{P_q}L^{\tau_q^{(p)}}$ with $L \geqslant 32$, expansion $N_y = 2$, and fixed $y = 0.75$. The horizontal line corresponds to $8\gamma = 0.01795$. For comparison, earlier data by Evers *et al.* [20] for $\Delta\tau_q$ is also shown (solid blue line and open symbols).

reasonable fit parameters for $0.5 \lesssim y \lesssim 1.0$. A set of fit parameters thus obtained for $\Delta\tau$ is displayed in Fig. 16. Based on the individual fit parameter $\Delta\tau_q$, the quartic scaling factor γ_q has been estimated; the result is also displayed in Fig. 16.

A remarkable property of the function γ_q thus obtained is its weak dependency on its argument $\gamma_q = \gamma$, with $8\gamma = 0.0178 \pm 0.0002$; the error bars are discussed in the Appendix, Sec. A 2. This observation motivates the definition of the scaling function

$$\tilde{F}_q(L) := F_q(L)/[(q-1)(q-2)]$$
$$\approx \tilde{F}_q(L_0) + \frac{x_q - x_q^{(p)}}{q(q-1)(q-2)(3-q)/8} \ln L/L_0$$
$$= \tilde{F}_q(L_0) + 8\gamma \ln L/L_0$$

plotted in Fig. 17. It displays the striking feature of all reciprocity pairs collapsing onto the same master curve, within the numerical error bars ("hypercollapse").
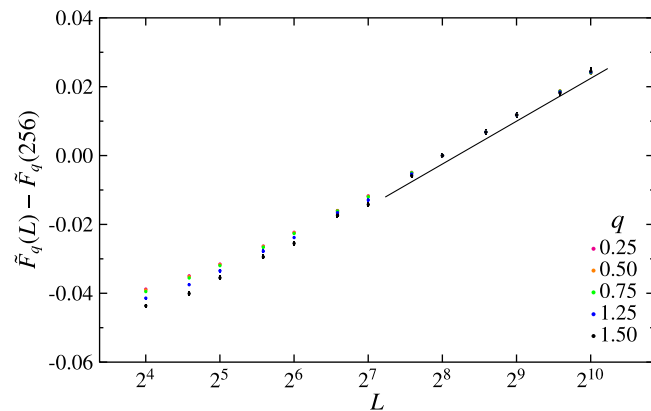

FIG. 17. The function $\tilde{F}_q(L)$ displays a nearly perfect scaling collapse for all q values listed ("hypercollapse"). The finite slope of this trace is a manifestation of quartic terms in the multifractal spectra. The hypercollapse indicates that corrections to quartic terms are very small in the regime of q values here considered.
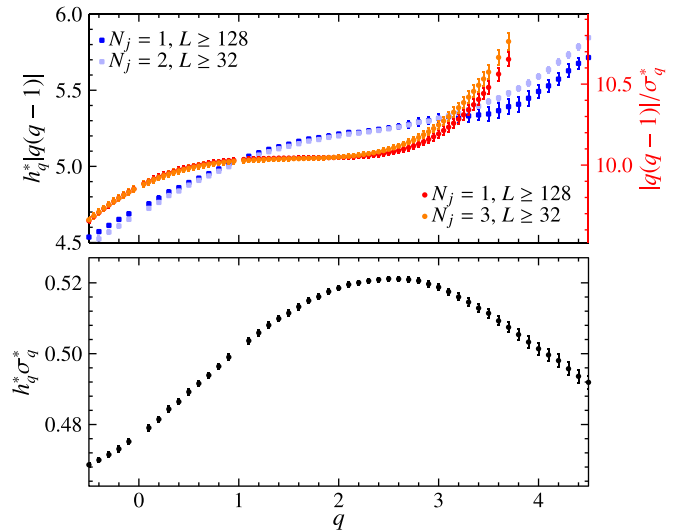

FIG. 18. Distribution height h_q^* and inverse width $1/\sigma_q^*$ as function of q. The scaling by $|q(q-1)|$ removes the trivial divergences and zeros at $q = 0, 1$. The two data sets are shown per observable in order to illustrate the goodness of the fitting (see Appendix, Sec. A 2). The lower panel shows the effective area $h_q^*\sigma_q^*$.

B. Width $\sigma_q(L)$ and height $h_q(L)$

As natural descriptor of the form of the distribution function $\mathcal{P}_q(\ln P_q; L)$ we have employed the second moment $\sigma_q(L)$ and the peak height $h_q(L)$. Following Eq. (10) we analyze the finite-size corrections for each q, thus estimating the fixed-point values σ_q^*, h_q^*. Figure 18 shows the height h_q and inverse width $1/\sigma_q$ as function of the moment q reduced by the behavior near $q = 0, 1$; by definition: $1/h_q^* = 0$, $\sigma_q^* = 0$. As readily seen from the data, the product $h_q^*\sigma_q^*$ depends on q. It thus is indicating a gradual change of the asymptotic shape of $\mathcal{P}_q$ with varying q.

C. Tail exponents

The evolution of the IPR distribution with q also manifests its asymptotic regime where it is described by a power law [1,23]

$$\tilde{\mathcal{P}}_q(P_q; L) \sim \mathcal{P}_q(\ln P_q; L)/P_q \sim P_q^{-1-\zeta_q} \tag{16}$$

with tail exponent ζ_q (see Figs. 3 and 19 for illustration). The asymptotic regime is given with $P_q/P_q^{\text{typ}} \ll 1$, $q \in (0, 1)$ and $P_q/P_q^{\text{typ}} \gg 1$ otherwise.

Typical and average IPR. For $\zeta_q > 1$, the first moment of the distribution exists, and hence the average $\overline{P_q}$ and the typical value P_q^{typ} show the same scaling with the system size. Contrary, at $\zeta_q < 1$ the moments will be dominated by the upper bound of the integral, which depends on L, so average and typical IPR will scale differently [1,23]. At the critical point $\zeta_{q^\pm} = 1$, which separates both regimes, the Legendre transformed τ_q vanishes, $f_{q^\pm} = 0$, where

$$f_q := q\frac{\partial \tau_q}{\partial q} - \tau_q = d + q\frac{\partial x_q}{\partial q} - x_q$$
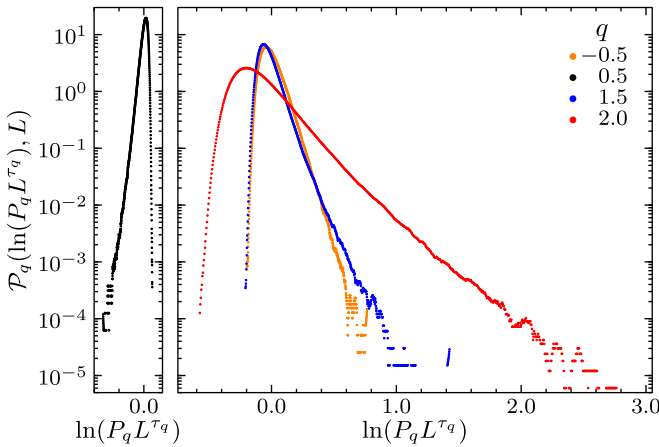$$= d - \frac{1}{8}q^2 - \gamma q^2(3q^2 - 12q + 11) + O(q^5). \tag{17}$$

FIG. 19. Distribution $\mathcal{P}_q(\ln[P_q(L)L^{\tau_q}];L)$ at $L = 1024$ for representative q values. The tail is seen to be approached from the peak value passing through an inflection point. Figure 20 zooms into the tail.

FIG. 21. Similar to Fig. 20, but for $q = \frac{1}{2}$ (left) and $q = 2$ (right) with $\zeta_{0.5} = -35(1)$ and $\zeta_2 = 4.5(1)$.

For $\gamma \geqslant 0$, the polynomial has two real roots ± 4 in the case $\gamma = 0$. For the realistic value $\gamma = \frac{1}{448}$, we obtain $q_-^* = -2.714$ and $q_+^* = 3.739$. We mention in passing that the freezing limit is given by $\partial\tau_q/\partial q = 0$; it describes the upper bound in q for the validity of Eq. (17) [1,23]. We estimate $q_c \approx 5.90$ for $8\gamma = 0.017\,86$, so the evolution at our considerations is safely away from this limit.

Numerical estimates. Figure 19 shows the tail of the distribution $\mathcal{P}_q$ and the corresponding inflection point for selected q values. A zoom-in on the corresponding tails is displayed in Figs. 20 and 21. The data shown in these figures highlight the difficulties encountered when trying to numerically estimate the tail exponent ζ_q: (i) The tail exhibits a slow evolution with increasing system size L tending towards decreasing slope. (ii) The power law is best developed far in the tails, where rare events prevail and statistical noise is large. When fitting the tail exponents, we have restricted the fitting window to the
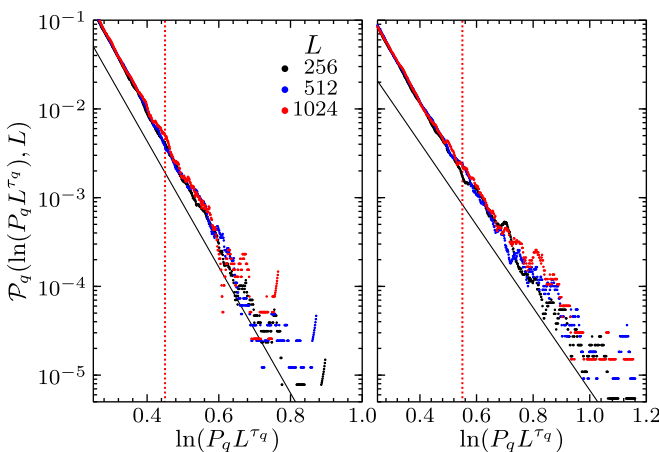
regime in $\mathcal{P}_q$ outside the inflection point. Because of (ii) the numerical error bars are sizable, because of (i) our estimate should be considered an upper bound, strictly speaking. The results for the tail exponents obtained in this way are given in Fig. 22.

Discussion. As seen already from the raw data, Fig. 19, ζ_q is a rapidly increasing function when approaching $q = 1$ from above. Moreover, it displays a change in sign at $q = 1$ and, similarly, also at $q = 0$. These observations have motivated us to plot in Fig. 22 the product $\zeta_q q(q - 1)$, which is always positive and appears to display a weaker dependency on q, at least for q values sufficiently far away from $q = 0, 1$. Near these particular values, ζ_q becomes very large and hence the numerical estimates carry very large error bars. At $q > 1$ the exponents ζ_q display the same qualitative behavior already known from other Anderson transitions [1]: ζ_q is decreasing with increasing q for $q > 1$.

FIG. 20. Evolution of the tails of the distribution $\mathcal{P}_q(\ln[P_q(L)L^{\tau_q}];L)$ with increasing system size $L = 256, 512, 1024$ at $q = -\frac{1}{2}, \frac{3}{2}$; raw data shown in Fig. 19. The solid lines indicate fitted power laws with $\zeta_{-0.5} = 10.7(4)$ and $\zeta_{1.5} = 16.4(4)$; the red dotted line indicates the fitting window.
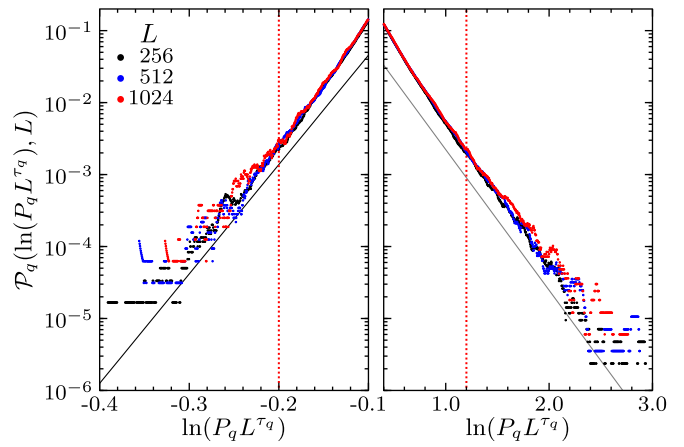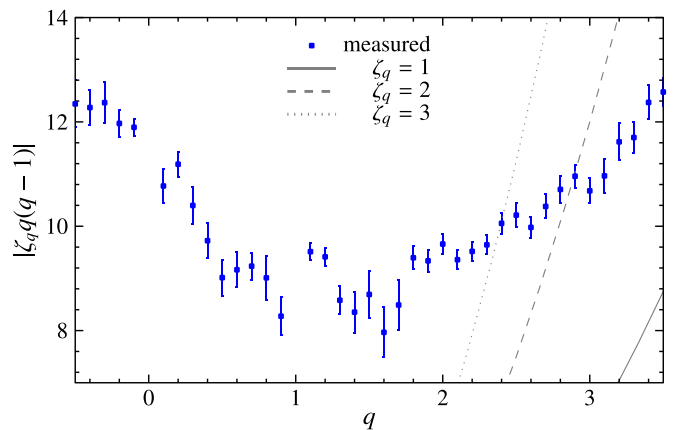

FIG. 22. Tail exponents ζ_q of the IPR distribution as defined in Eq. (16). Three lines are also shown. There intersection with the data trace indicates the q value at which the tail exponent takes values $\zeta_q = 1, 2, 3$. At q values larger than these the first, second, and third moments of the IPR will be dominated by the integral boundaries rather than by the bulk of the distribution.
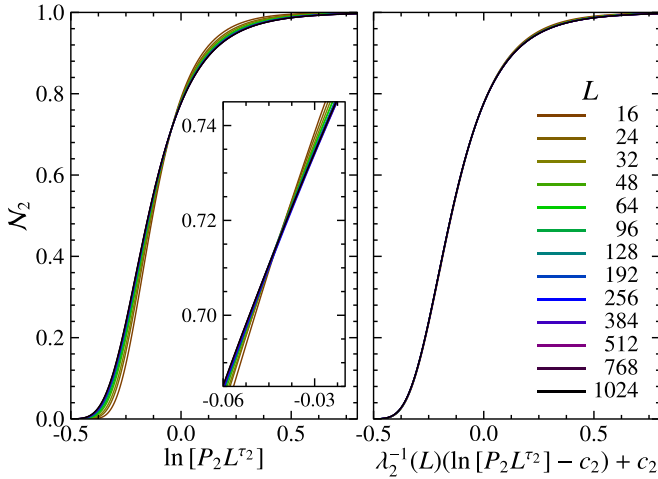
FIG. 23. Integrated distribution $\mathcal{N}_2(\ln[P_2(L)L^{\tau_2}];L)$ before (left) and after (right) abscissa rescaling about the common intersection point $c_2 = -0.042 \pm 0.004$. Inset: vicinity of the crossing point. The scale parameter abbreviates $\lambda_2(L) := h_2^*/h_2(L)$ with $h_2(L)$ given in Fig. 2.
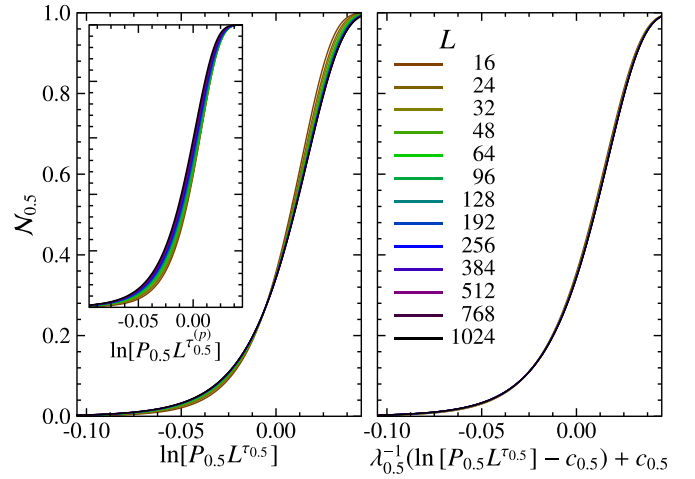

FIG. 24. Similar to Fig. 23 but for $q = \frac{1}{2}$ with the common intersection point $c_{0.5} = -0.005 \pm 0.002$. Inset: integrated distributions as they would have been obtained with $\gamma = 0$, i.e., $\mathcal{N}_{0.5}(\ln[P_{0.5}(L)L^{\tau_{0.5}^{(p)}}];L)$. The plot highlights the importance to account for quartic corrections to τ_q to achieve the data collapse seen in the right-hand-side panel.

V. COLLAPSE OF FINITE-SIZE DISTORTED DISTRIBUTION FUNCTIONS

The shape of the distribution function $\mathcal{P}_q(\ln P_q(L)L^{\tau_q}; L)$ exhibits sizable finite-size effects seen, for instance, in Figs. 1, 5, and 8. In this section we present a heuristic single-parameter rescaling of this distribution to the effect that all traces seen, e.g., in Fig. 1, collapse onto a single master curve.

A. Single-parameter rescaling of distribution functions

We consider the integrated distribution function

$$\mathcal{N}_q(\ln[P_q(L)L^{\tau_q}]; L) := \int_{-\infty}^{\ln P_q L^{\tau_q}} dx\, \mathcal{P}_q(x; L), \qquad (18)$$

so $\mathcal{P}_q(x; L) = \partial_x \mathcal{N}_q(x; L)$. The species corresponding to $q = 2$ is depicted in Fig. 23 and $q = \frac{1}{2}$ in Fig. 24. The data are seen to exhibit a common crossing point, e.g., $\ln P_2 L^{\tau_2} \approx -0.042 \pm 0.004$ in Fig. 23. Clearly, the existence of a crossing point of a pair of traces corresponding to two neighboring system sizes is expected. Also expected is a flow of the crossing point with increasing system sizes towards a limiting value. Therefore, it is remarkable that there is virtually no such flow discernible in the inset of Fig. 23 even though the raw data, Fig. 1, do exhibit sizable finite-size effects of the order of 20%.

The stability of the crossing point allows for an attempt at a single-parameter rescaling of the abscissa in Fig. 23 with the crossing point c_q being the fixed reference position:

$$\mathcal{N}_q(\Lambda_q(L); L) = \mathcal{N}_q^\infty(\lambda_q^{-1}(L)\{\Lambda_q(L) - c_q\} + c_q), \qquad (19)$$

where $\Lambda_q(L) := \ln[P_q(L)L^{\tau_2}]$. A natural choice for the scale factor $\lambda_q(L)$ here introduced would be the (inverse) slope at the crossing point. We note that in Fig. 23 the crossing point turns out to be very close to the inflection point, where the slope is given by the height $h_q(L)$. With this observation, we adopt the definition $\lambda_q(L) := h_q^*/h_q(L)$ constructed so that $\lambda_q^* = 1$.

As is demonstrated in Fig. 23, left panel, the rescaled integrated distribution function (19) for $q = 2$ exhibits a nearly perfect collapse towards a master curve in a window of system sizes L, that covers almost two decades. This is highly remarkable because apart from reading out $h_q(L)$ in Fig. 1 there is no fitting parameter involved. Only at larger arguments deviations from the master curve are visible for the smallest system sizes.

A collapse of similar quality can be obtained also at other q values, e.g., for $q = \frac{1}{2}$ as demonstrated in Fig. 24. As also shown for this case, a collapse can only be achieved if quartic terms in τ_q are accounted for: when stipulating $\gamma = 0$ traces corresponding to different system sizes do not exhibit the crossing point (inset Fig. 24).

Further discussion. To further investigate the heuristic rescaling we here propose, we plot in Fig. 25 the distribution functions shown in Fig. 3 after rescaling, which correspond to the derivative of the traces shown in Fig. 23, right: while the collapse in the bulk of the distribution function is close to perfect, deviations in the tail can be seen also here.

The single-parameter ansatz (19) implies for the distribution function Eq. (6), i.e.,

$$\mathcal{P}_q(\Lambda_q; L) = \frac{\lambda_q^*}{\lambda_q} \mathcal{P}_q^\infty \left(\frac{\lambda_q^*}{\lambda_q} \{\Lambda_q - c_q\} + c_q \right),$$

where the dependency of $\Lambda_q(L)$ and $\lambda_q(L)$ on L has been suppressed in our notation. The expression allows for an interpretation of finite-size corrections as far as they affect the bulk of the distribution rather than its tail; they manifest as a "dressing" of the reduced IPR amplitudes

$$P_q L^{\tau_q} e^{-c_q} \rightarrow [P_q L^{\tau_q} e^{-c_q}]^{\lambda_q^*/\lambda_q}. \qquad (20)$$

For the average amplitude we thus derive

$$\overline{P_q L^{\tau_q}}(L) = e^{(\lambda_q^*/\lambda_q - 1)c_q} \int dx\, e^{\lambda_q x} \mathcal{P}_q^\infty(x). \qquad (21)$$
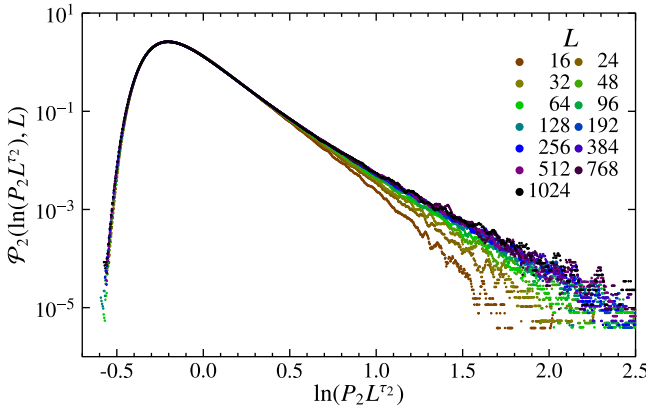
FIG. 25. Distribution function $\mathcal{P}_q$ shown in Fig. 3 here after performing the single-parameter scaling transformation. The traces correspond to the derivative of the integrated distribution $\mathcal{N}_q$ shown in Fig. 23 [see Eq. (18)]. The plot highlights the excellent collapse seen in the bulk of the distribution and the lack thereof in the tails.

Upon expanding the right-hand side of Eq. (21) in $\lambda_q(L) - \lambda_q^*$ we recover the form (14). Judging from the excellent collapse achieved in Figs. 23 and 25, the expression appears to have the advantage that it partially resums the higher-order terms in (14).

B. Exponent fittings via Kolmogorov-Smirnov test

The preceding analysis of the flow of distribution functions motivates a fresh approach towards estimating multifractal spectra τ_q in the presence of strong finite-size corrections. Based on field-theoretic arguments [25,26], the conventional method follows Eq. (14) fitting the average IPR, $\overline{P}_q(L)$, with a leading power and subleading corrections [1]. From a computational perspective, a frequent problem with this procedure is that fits are unstable due to a proliferating number of fitting parameters.

Method. We here propose an alternative method for estimating exponents τ_q. It is simple and as compared to the conventional approach it has the dramatic advantage that except for τ_q there is no other parameter that requires optimization. The main idea is to define a family of auxiliary functions

$$\mathcal{N}_q(\ln[P_q(L)L^\tau]; L),$$

with family parameter L; examples for two families that differ by the choice of τ have been depicted in Fig. 24. With increasing L, family numbers become more and more indistinguishable, if and only if τ coincides with τ_q. To monitor this evolution we define a distance between two family members:

$$\mathfrak{D}_q(L, L'; \tau) = \max\left[\mathcal{N}_q\left(\Lambda_q^\tau(L); L\right) - \mathcal{N}_q\left(\Lambda_q^\tau(L'); L'\right)\right], \tag{22}$$

where we have abbreviated $\Lambda_q^\tau(L) := \ln[P_q(L)L^\tau]$. We employ this particular measure of closeness because it allows us to adopt the Kolmogorov-Smirnov test [16] to assess the statistical significance, traditionally called α, of a distance obtained for a pair of two numerical data

TABLE I. Number of lattice realizations N_{samples} (in units of 1000) as function of system size L.

L	16	24	32	48	64	96	128
$N_{\text{samples}}(L)$	9216	6136	6000	6144	6750	6000	6000
L	192	256	384	512	768	1024	
$N_{\text{samples}}(L)$	6144	5582	5121	3632	2710	1930	

sets:

$$
\begin{aligned}
&\alpha_q(L, L', \tau) \\
&= 2\exp\left(-\frac{2N_{\text{samples}}(L)N_{\text{samples}}(L')}{N_{\text{samples}}(L) + N_{\text{samples}}(L')}\mathfrak{D}_q^2(L, L'; \tau)\right),
\end{aligned} \tag{23}
$$

where N_{samples} denotes the number of disorder configurations in the ensemble (see Table I). The "best guess" for τ_q is given by the parameter τ that minimizes the distance between two neighboring pairs L, L' in the large-L limit taken at L'/L fixed. A data point for the distance will be accepted if the corresponding significance is better than a predefined level, e.g., 1%: $\alpha \lesssim 0.01$. As an illustration, Fig. 26 displays the typical evolution of $\mathfrak{D}_q(L, 2L; \tau)$ with increasing system size. Here a quartic term manifests as the superior choice as compared to a parabolic spectrum $\gamma = 0$.

Discussion. The proposed approach to estimating τ_q operates by choosing a guess that brings the system-size flow of $\mathcal{P}_q(\ln P_q L^\tau)$ to a standstill in the limit of large L. The advantage of this approach is that the goodness of the guess can be read of from Fig. 26 without fitting: worse guesses reveal themselves as compared to the better ones by leveling off to saturated values of the pair distance $\mathfrak{D}_q(L, L'; \tau)$. Using this technique we arrive at an estimate $8\gamma_{1/2}=0.0175\pm0.0010$.

VI. SUMMARY AND OUTLOOK

The main goal of this work was to present an in-depth analysis of multifractality and finite-size corrections for the class C quantum Hall transition that could serve as a paradigm for similar investigations in other symmetry classes. The symmetry class C lends itself most naturally for this purpose because out of the full spectrum τ_q two nontrivial exponents, i.e., $q = 2, 3$, are known analytically and therefore can serve as a reference point for studying finite-size effects.

As compared to most earlier studies, our investigation has not focused on average inverse participation ratios $\overline{P}_q(L)$, but rather on the flow with system size L of the entire distribution function $\mathcal{P}_q(\ln P_q; L)$. As it turns out, the shape of this function as far as its bulk is concerned is conveniently parametrized by a single parameter, e.g., its peak value $h_q(L)$. We observe that the distribution $\mathcal{P}_q$ exhibits a scaling form that accounts for finite-size corrections with τ_q and $h_q(L)$ as the only input parameters.

Embarking on this result, we have explored the potential of a different approach to finite-size corrections based on the Kolmogorov-Smirnov test. The method is sufficiently sensitive to allow us extracting τ_q essentially without any fitting to an accuracy good enough in order to reliably detect
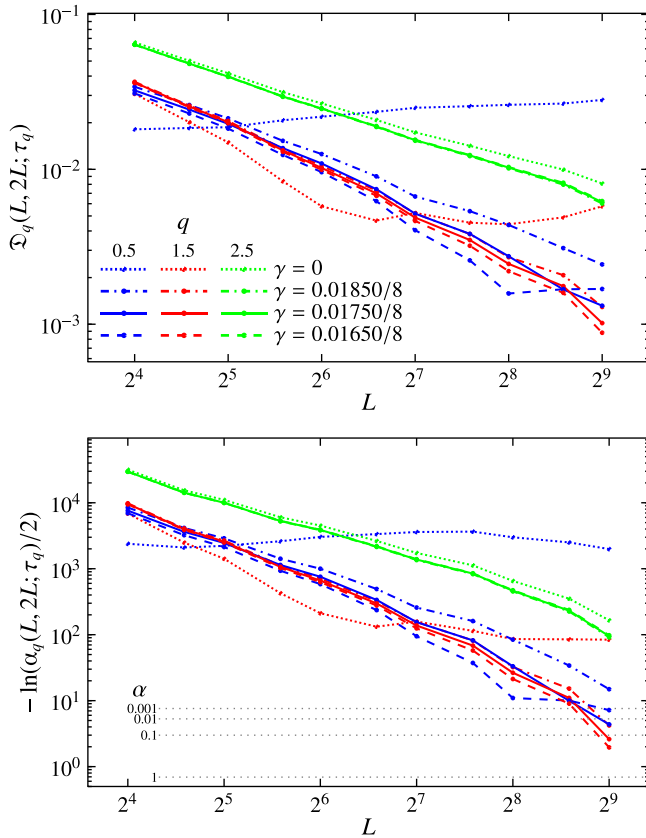
FIG. 26. Estimating the spectrum τ_q adopting the Kolmogrov-Smirnov test. Upper panel: distance for a pair of IPR distributions $\mathfrak{D}_q(L, 2L; \tau_q)$, defined in Eq. (22) at system sizes L and $2L$ for different τ_q "guesses" with and without quartic terms: $\gamma = 0$ (dashed lines) and $8\gamma = 0.01750$ (solid lines). The "best estimates" for τ_q are those with smallest distances at largest system sizes. Lower panel: significance level $\alpha_q(L)$ as given in Eq. (23) for every distance given in the upper panel. The horizontal line indicates significance levels of 0.1%, 1%, and 10% ($\alpha = 10^{-3}, 10^{-2}, 10^{-1}$).

nonparabolic components in τ_q: $\Delta\tau_q := \gamma_q q(q-1)(q-2)(q-3)$. We obtain that γ_q is essentially independent of q with $8\gamma = 0.0178 \pm 0.0010$ for $q \in (-0.5, 3)$. This outcome satisfies the reciprocity symmetry.

We have confirmed these results by performing a standard analysis of finite-size corrections based on fitting $\overline{P}_q(L)$ to a leading power law and irrelevant corrections: $\sim L^{-\tau_q}[1 + O(L^{-y})]$; irrelevant scaling indices could be reliably determined, $y \approx 0.9 \pm 0.3$ within a window $q \in (-0.5, 2)$; the large-q bound is imposed by the loss of numerical stability at $q \gtrsim 2$. The origin of this loss has been traced back to the tail of the IPR distribution function; it is characterized by an exponent ζ_q which falls below two, $\zeta_q < 2$, at $q > q_+^*$, so that the second moment of the IPR distribution is dominated by integral boundaries. The overall analysis fully confirms that terms of higher order than quartic are strongly suppressed in τ_q.

The versatile analysis techniques presented in this work are designed to readily carry over to other critical points. As an outlook, we mention that the quantum Hall transitions in symmetry classes A [3,4] and AIII [27] experience a resur-
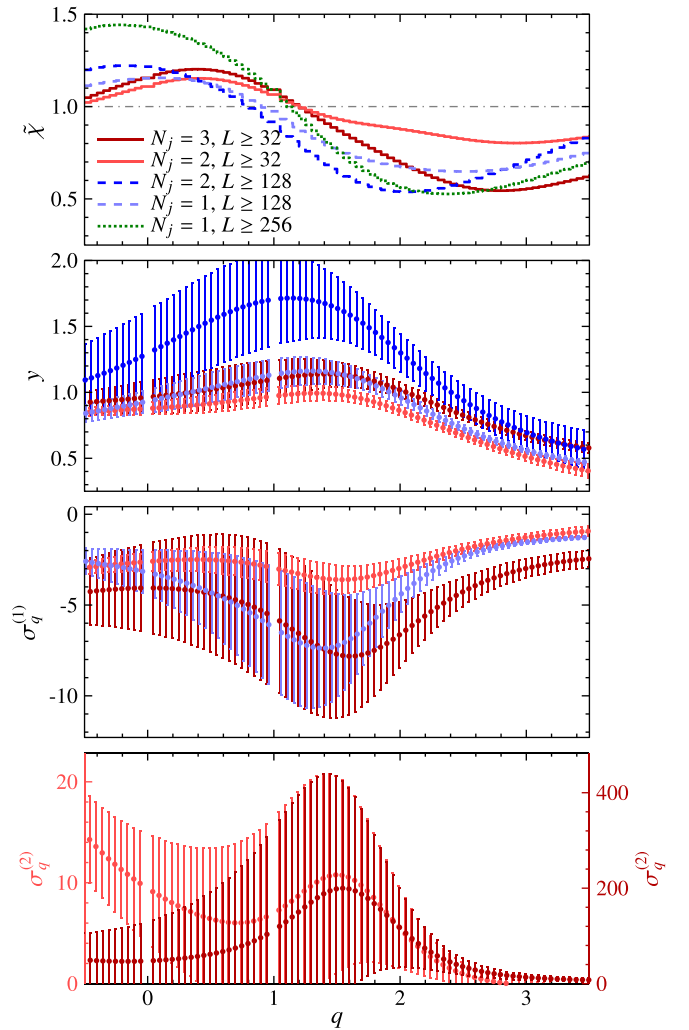

FIG. 27. Parameters following Eq. (11) from fitting to $\sigma_q(L)$ data analogous to Figs. 2 and 6. Estimates of the goodness of fit $\tilde{\chi}_q$ (top panel), irrelevant exponent y (second panel), and amplitudes $\sigma_q^{(1,2)}$ (lower panel) are given for several fits with expansion order N_y and system size L.

gence of attention, recently. It will be highly interesting to compare the critical behavior of these transitions that has been addressed previously by Evers *et al.* [28] and Obuse *et al.* [29] in greater depth, e.g., with respect to finite-size corrections on distribution functions and with akin eye on the identification of the critical field theory. Further, the Kolmogorov-Smirnov test advocated in this work as a methodological development is not without alternative in mathematical statistics. We here have to leave it to future work to unravel the full potential of this analysis method in the context of scaling and critical behavior near Anderson and quantum Hall transitions.

ACKNOWLEDGMENTS

APPENDIX

1. Sample statistics

Table I lists the number of samples, N_{samples}, for all (linear) system sizes L considered. A number of $N_{\text{ev}} = 6$ eigenvectors have been calculated per sample with eigenvalues taken closest to unity. In a separate set of test calculations with $N_{\text{ev}}=4, 6, 12$ we have ascertained that our results are not sensitive to the choice of N_{ev}; for a given disorder realization, the results for the IPR agree to an accuracy better than 11 relevant digits at $L = 128$.

For the statistics shown in the main paper only the eigenvector with eigenvalue closest to unity has been considered. As we show in Sec. A 3, the other eigenvectors exhibit significantly larger finite-size corrections and therefore have been discarded from the main analysis.

2. Details on the finite-size scaling analysis

a. Irrelevant scaling corrections: estimating y

Corrections to scaling of the observables $\sigma_q(L)$ and $h_q(L)$ have been analyzed based on the expansion (10), i.e.,

$$\sigma_q = \sigma_q^* \left(1 + \sum_{j=1}^{N_y} \sigma_q^{(j)} L^{-jy}\right),$$

where N_y denotes the expansion order. For assessing uncertainties in fitting parameters related to statistical and systematic errors, different combinations of regimes in L and $N_y \leqslant 3$ have been considered, as well as fits with y kept adjustable or fixed. Both observables σ_q and h_q show a similar behavior with respect to the irrelevant exponent y as well. We here focus on the σ_q-based data.

In Fig. 27, we display the fitting parameters, goodness of the fit $\tilde{\chi}$, exponent y, and two amplitudes $\sigma^{(1,2)}$, for various fitting conditions. The estimates of different fits agree well with the error bars; the goodness of fit suggests that best results are obtained for $(N_y = 2; L = 32)$ and $(1; 128)$. The results of Fig. 27 are consistent with (11) for $q \lesssim q_+^*$, $q_+^* \approx 2.7$ in the sense that in this regime the fit for y is nearly the same for each moment q. At $q \gtrsim q_+^*$, fits deviate from this expectation. Finite-size effects proliferate, which reflects in the fitting as estimates for y reducing by a factor of 2; the respective amplitudes $\sigma_q^{(1,2)}$ keep moderate values (see Fig. 27).

In order to explore the possibility of getting good fits with y value situated in the interval $y \in [0.75, 1.25]$ also at $q \gtrsim q_+^*$, we have made further tests. The results for the fitting parameters have been displayed in Fig. 28, where the cases $y = 0.75, 1.0$ are compared. As is seen from the goodness of
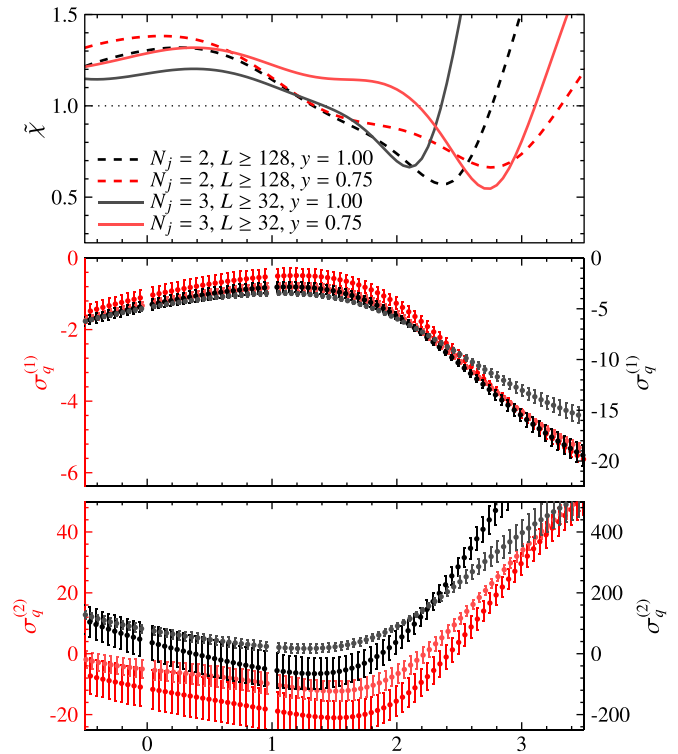

FIG. 28. Fit quality $\tilde{\chi}$ as function of the moment q for a q-independent irrelevant exponent y for several fits with expansion order N_y and data ranges. Similar to the previous Fig. 27, the plot highlights that beyond a moment q_+^* finite-size corrections no longer follow the canonical expansion (12).

fit, Fig. 28 top panel, including higher orders in L^{-y} does not seem to properly describe the finite-size effects in the regime $q \gtrsim q_+^*$.

Taken at face value, the finite-size corrections to the variance appear to change their nature for moments crossing the point $q \approx q_+^*$. We interpret this observation with an eye on the tail of the distribution function $\mathcal{P}_q(P_q; L)$ discussed in Sec. IV C. The variance σ_q as defined in Eq. (9) requires the calculation of the second moment of the distribution, which exists only if $\zeta_q \geqslant 2$. The observation suggests a precise definition of $\zeta_{q_+^*} = 2$, yielding an estimate $q_+^* \approx 2.7$ based on the results of Fig. 22. This estimate is consistent with the apparent decrease of y that we witness in Figs. 27 and 28. We mention that a moment similar to q_+^*, which is associated with the IPR variance, exists also for the IPR average. It is defined as $\zeta_{q_+} = 1$; at $q > q_+$ average and typical IPR cease to scale alike with system size [1].

b. Estimating γ upon including corrections to scaling

We perform an analysis of finite-size effects following the conventional expansion Eq. (10) for the average IPR $\overline{P_q}$. The main goal is to quantify deviations from parabolicity, $\delta\tau_q = \delta x_q$, including finite-size corrections. Since above analysis suggest a fixed exponent $y \approx 1$ only for moments $q < q_+^*$, we compare fits involving a range $y \in \{0.5, 0.75, 1.0\}$. Figure 29 shows the multifractal exponent τ_q obtained from such fits, represented as deviation from parabolicity $\Delta\tau_q := \tau_q - \tau_q^{(p)}$.
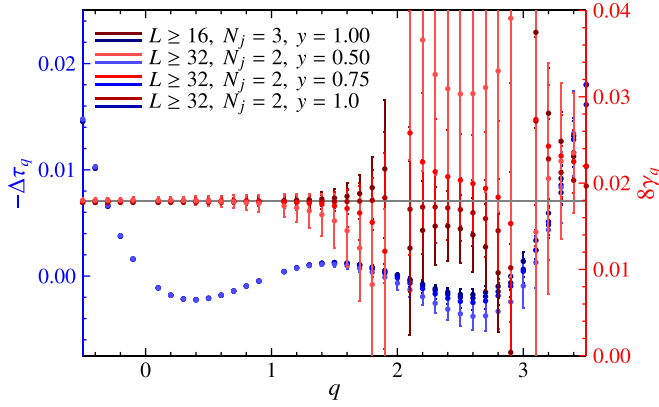
FIG. 29. Estimate of the nonparabolic multifractal content $\Delta\tau_q := \tau_q - \tau_q^{(p)}$ and the corresponding quartic curvature γ_q as function of q. Fits are based on $\overline{P_q} L^{\tau_q^{(p)}}$ for several fit and parameter ranges. The horizontal line marks $8\gamma = 0.01795$.

As one would expect based on the analysis of $\sigma_q(L)$ above, fitting gives consistent results for $\Delta\tau_q$ in the regime $q \lesssim 2$. The resulting curvature amounts to $8\gamma \approx 0.0179$ with small statistical error bars that, however, exhibit a significant q dependence. We estimate $8\gamma = 0.0178 \pm 0.0012$ based on the error bars we obtain near $q \approx 0$.

With q approaching $q_+^* \approx 2.7$ from below, the error bars are seen to proliferate dramatically. Importantly, within the error bars the reciprocity relation $\Delta\tau_q = \Delta\tau_{3-q}$ is seen to be fulfilled in the range of moments investigated $-\frac{1}{2} \lesssim q \lesssim 3.5$.

3. Eigenvectors at neighboring energies

Per sample we calculate three pairs of eigenvectors with eigenvalues nearest to unity (see Sec. A 1). The results in the main paper include only one of these wave functions, i.e., the one with eigenvalue closest to unity. We here present a brief analysis of the properties of the other two wave functions with eigenvalues next nearest and next-next nearest to unity.

Figure 30 shows the scaled IPR distribution function $\mathcal{P}_q(\ln[P_q(L)L^{\tau_q}]; L)$ at $q = \frac{1}{2}$ for all three eigenstates taken
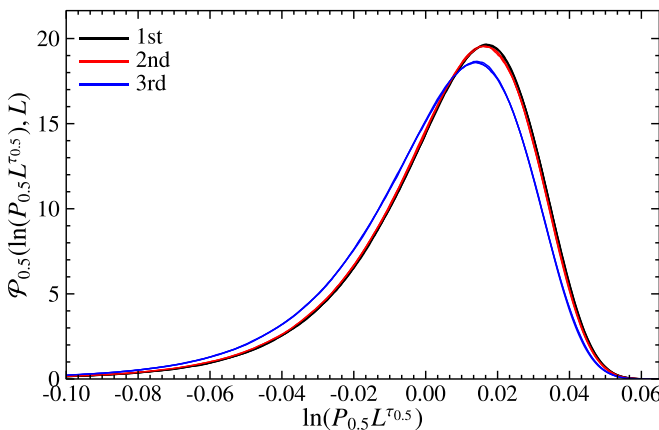

FIG. 30. Distribution functions $\mathcal{P}_{0.5}(\ln[P_{0.5}(L)L^{\tau_{0.5}}]; L)$ for $q = 0.5$ and $L = 512, 768, 1024$ obtained for three sets of eigenstates.
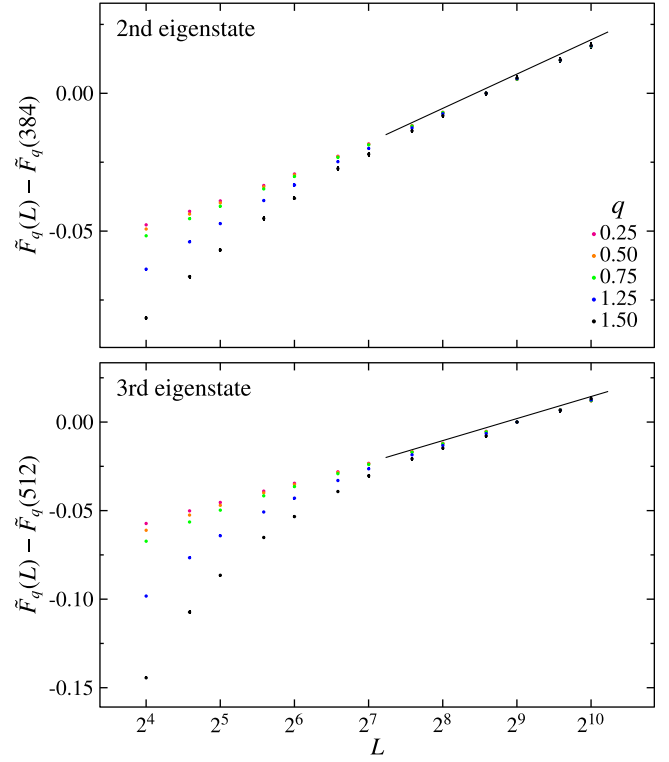

FIG. 31. Similar to Fig. 17, but for the eigenstates with eigenvalues second nearest (upper panel) and third nearest (lower panel) to unity. The "hypercollapse" happens at a larger length scale; we changed the reference length L_0 to 384 and 512 for second and third eigenstate, respectively. The slopes of the guiding lines on both panels as well as in Fig. 17 are equal.

at $8\gamma = 0.00178$. The excellent data collapse illustrates that τ_q is the same for all three energies, despite the fact that $\mathcal{P}_q$ is not. The collapse is illustrated for a wider range of q values in Fig. 31. It displays the auxiliary quantity $\tilde{F}_q(L)$ for the second and third closest eigenstates. Similar to the case of the first eigenvector, Fig. 17, also the second and third nearest eigenstates exhibit the hypercollapse. However, for these eigenvectors the finite-size effects turn out to be stronger; the collapse is seen to occur only at larger system sizes, i.e., above $L = 384$ or 512.

4. IPR dependence on microscopic definition

By definition, the IPR is a sum over space of a local measure $\mu(\mathbf{r})$ taken to the power q: $\int d\mathbf{r}\,\mu(\mathbf{r})^q$. The definition employed in Eq. (8) on the lattice amounts to $\mu_l = \sum_\sigma |\psi_{l\sigma}|^2$.

TABLE II. Number of lattice realizations N_{samples} (in units of 1000) as a function of system size L for the test calculation regarding the microscopic definition.

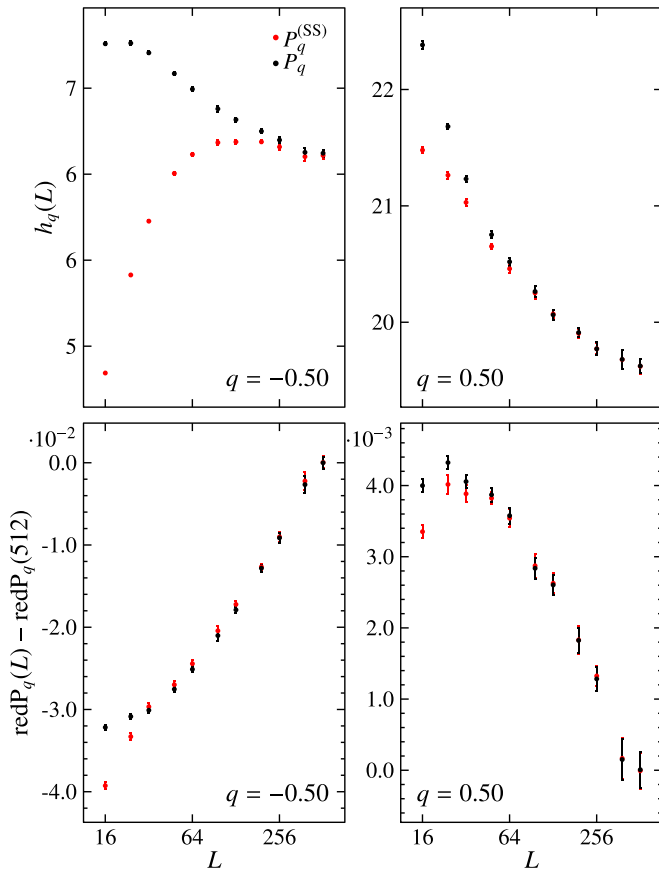| L	16	24	32	48	64	96	128
$N_{\text{samples}}(L)$	5000	5000	5000	5000	5000	1081	2518
L	192	256	384	512	768	1024	
$N_{\text{samples}}(L)$	2383	1558	393	582			

FIG. 32. Lower panels show the flow of the height $h_{0.5}(L)$ and maximum position $\mathrm{redP}_{0.5}(L)$ as function of L. The latter is shown with respect to the position of the largest system $L = 512$. The collapse for $L \geqslant 64$ emphasizes the independence on the microscopic details.

An alternative local measure is given by $\mu_l = |\psi_{l\sigma}|^2$, so the statistical properties of the spin density are evaluated for each component, separately. The local density of a given spin direction is more sensitive to rare events as compared to the local number density. We here present a sanity check indicating that the multifractal spectrum is not affected by this difference, at least not in the q window of most interest to us.

We define the spin-separated IPR

$$P_q^{(\mathrm{SS})}(L) = \sum_l \sum_\sigma |\psi_{l\sigma}|^{2q}. \tag{A1}$$

We have as usual $P_{q=1}^{(\mathrm{SS})} = 1$ from normalization, while $P_{q=0}^{(\mathrm{SS})} = 2L^2$ as opposed to $P_{q=0} = L^2$; the definition of τ_q is unaffected by this detail. Qualitative deviations between the scaling properties of P_q and $P_q^{(\mathrm{SS})}$ are expected for q approaching more and more negative values.

To illustrate similarities and dissimilarities, we have performed a separate study considering systems up to linear system size $L = 512$ (see Table II for the sample statistics). The results of these calculations are summarized in Fig. 32 for the paradigmatic cases $q = \pm\frac{1}{2}$. The plot allows us to draw several conclusions. (i) At positive q, the distributions of P_q and $P_q^{(\mathrm{SS})}$ exhibit a very similar shape, represented by $h_q(L)$ in the top row of Fig. 32. Likewise, the evolution of the distributions with increasing system size is the same, confirming the same set of multifractal indices $\tau_{1/2}$. Corresponding evidence is given in Fig. 32; lower row that shows the flow the peak position of the reduced distributions $\mathcal{P}_q(\ln P_q L^{\tau_q^{(\mathrm{p})}})$ and $\mathcal{P}_q(\ln P_q^{(\mathrm{SS})} L^{\tau_q^{(\mathrm{p})}})$: after performing a rigid shift both traces collapse indicating that the critical exponent is the same for both measures. (ii) With respect to the critical exponent the situation is seen to be similar at $q = -\frac{1}{2}$, as illustrated in the bottom row of Fig. 32. The form of the distribution functions begins to change shape, however, as clearly displayed in Fig. 32 (top row) by $h_{-1/2}(L)$. We take this observation as a precursor for a qualitative deviation of the critical behavior occurring at more negative q values.

[1] F. Evers and A. D. Mirlin, Anderson transitions, Rev. Mod. Phys. **80**, 1355 (2008).

[2] M. R. Zirnbauer, Conformal field theory of the integer quantum hall plateau transition, arXiv:hep-th/9905054.

[3] R. Bondesan, D. Wieczorek, and M. Zirnbauer, Gaussian free fields at the integer quantum hall plateau transition, Nucl. Phys. B **918**, 52 (2017).

[4] M. R. Zirnbauer, The integer quantum hall plateau transition is a current algebra after all, Nucl. Phys. B **941**, 458 (2019).

[5] H. Obuse, A. R. Subramaniam, A. Furusaki, I. A. Gruzberg, and A. W. W. Ludwig, Multifractality and Conformal Invariance at 2D Metal-Insulator Transition in the Spin-Orbit Symmetry Class, Phys. Rev. Lett. **98**, 156802 (2007).

[6] I. A. Gruzberg, A. W. W. Ludwig, A. D. Mirlin, and M. R. Zirnbauer, Symmetries of Multifractal Spectra and Field Theories of Anderson Localization, Phys. Rev. Lett. **107**, 086403 (2011).

[7] A. D. Mirlin, Y. V. Fyodorov, A. Mildenberger, and F. Evers, Exact Relations Between Multifractal Exponents at the Anderson Transition, Phys. Rev. Lett. **97**, 046803 (2006).

[8] I. A. Gruzberg, A. D. Mirlin, and M. R. Zirnbauer, Classification and symmetry properties of scaling dimensions at anderson transitions, Phys. Rev. B **87**, 125144 (2013).

[9] A. D. Mirlin and Y. V. Fyodorov, Distribution of Local Densities of States, Order Parameter Function, and Critical Behavior Near the Anderson Transition, Phys. Rev. Lett. **72**, 526 (1994).

[10] Y. V. Fyodorov and D. V. Savin, Statistics of impedance, local density of states, and reflection in quantum chaotic systems with absorption, J. Exp. Theor. Phys. Lett. **80**, 725 (2004).

[11] Y. V. Fyodorov, D. V. Savin, and H.-J. Sommers, Scattering, reflection and impedance of waves in chaotic and disordered systems with absorption, J. Phys. A: Math. Gen. **38**, 10731 (2005).

[12] A. D. Mirlin, F. Evers, and A. Mildenberger, Wavefunction statistics and multifractality at the spin quantum Hall transition, J. Phys. A: Math. Gen. **36**, 3255 (2003).

[13] I. A. Gruzberg, A. W. W. Ludwig, and N. Read, Exact Exponents for the Spin Quantum Hall Transition, Phys. Rev. Lett. **82**, 4524 (1999).

[14] V. Kagalovsky, B. Horovitz, Y. Avishai, and J. T. Chalker, Quantum Hall Plateau Transitions in Disordered Superconductors, Phys. Rev. Lett. **82**, 3516 (1999).

[15] F. Wegner, Inverse participation ratio in $2 + \epsilon$ dimensions, Z. Phys. B **36**, 209 (1980).

[16] M. H. DeGroot and M. J. Schervish, *Probability and Statistics*, 4th ed. (Pearson Education, Essex, England, 2012).

[17] J. T. Chalker and P. D. Coddington, Percolation, quantum tunnelling and the integer Hall effect, J. Phys. C: Solid State Phys. **21**, 2665 (1988).

[18] T. Senthil, J. B. Marston, and M. P. A. Fisher, Spin quantum hall effect in unconventional superconductors, Phys. Rev. B **60**, 4245 (1999).

[19] E. J. Beamond, J. Cardy, and J. T. Chalker, Quantum and classical localization, the spin quantum Hall effect, and generalizations, Phys. Rev. B **65**, 214301 (2002).

[20] F. Evers, A. Mildenberger, and A. D. Mirlin, Multifractality at the spin quantum Hall transition, Phys. Rev. B **67**, 041303(R) (2003).

[21] R. Klesse and M. Metzler, Universal multifractality in quantum Hall systems with long-range disorder potential, Europhys. Lett. **32**, 229 (1995).

[22] R. Klesse and M. Metzler, Modeling disoder quantum systems with, Int. J. Mod. Phys. C **10**, 577 (1999).

[23] A. D. Mirlin and F. Evers, Multifractality and critical fluctuations at the anderson transition, Phys. Rev. B **62**, 7920 (2000).

[24] H. Obuse, S. Bera, A. W. W. Ludwig, I. A. Gruzberg, and F. Evers, Statistics of conductances and subleading corrections to scaling near the integer quantum Hall plateau transition, Europhys. Lett. **104**, 27014 (2013).

[25] F. J. Wegner, The critical state, general aspects, in *Phase Transitions and Critical Phenomena*, Vol. 6, edited by C. Domb and M. Green (Academic, London, 1976).

[26] J. Cardy, *Scaling and Renormalization in Statistical Physics*, Cambridge Lecture Notes in Physics (Cambridge University Press, Cambridge, 1996).

[27] B. Sbierski, J. F. Karcher, and M. S. Foster, Spectrum-Wide Quantum Criticality at the Surface of Class AIII Topological Phases: An "Energy Stack" of Integer Quantum Hall Plateau Transitions, Phys. Rev. X **10**, 021025 (2020).

[28] F. Evers, A. Mildenberger, and A. D. Mirlin, Multifractality at the Quantum Hall Transition: Beyond the Parabolic Paradigm, Phys. Rev. Lett. **101**, 116803 (2008).

[29] H. Obuse, I. A. Gruzberg, and F. Evers, Finite-Size Effects and Irrelevant Corrections to Scaling Near the Integer Quantum Hall Transition, Phys. Rev. Lett. **109**, 206804 (2012).